https://doi.org/10.1016/j.nanoen.2021.105909



# A chemical etching strategy to improve and stabilize $RuO_2$-based nanoassemblies for acidic oxygen evolution

*Qing Yao,[†,#] Bolong Huang,[‡,#] Yong Xu,[§,#,*] Leigang Li,[†] Qi Shao[†] and Xiaoqing Huang[†,¶,*]*

[†]College of Chemistry, Chemical Engineering and Materials Science, Soochow University, Jiangsu 215123, China.

[‡]Department of Applied Biology and Chemical Technology, Hong Kong Polytechnic University, Hung Hom, Kowloon, Hong Kong SAR, China.

[§]Guangzhou Key Laboratory of Low-Dimensional Materials and Energy Storage Devices, Collaborative Innovation Center of Advanced Energy Materials, School of Materials and Energy, Guangdong University of Technology, Guangzhou, 510006, Guangdong, China.

[¶]College of Chemistry and Chemical Engineering, Xiamen University, Xiamen, 361005, China.

[#]These authors contributed equally.

[*]E-mail: yongxu@gdut.edu.cn; hxq006@suda.edu.cn or hxq006@xmu.edu.cn

**Keywords:** Ruthenium, Vacancy, Defect, Acidic, Oxygen Evolution Reaction

**Abstract:** $RuO_2$-based catalysts have been widely used for acidic oxygen evolution reaction (OER), a key half reaction of overall water splitting. However, $RuO_2$ suffers from the drawbacks of inferior OER performance in acidic conditions due to its poor stability. We here demonstrate a chemical etching strategy for fabricating a Ru/Fe oxide towards OER, in which Fe species in the pristine Ru/Fe nanoassemblies (P-Ru/Fe NAs) are partially etched by nitric acid ($HNO_3$), leading to the generation of abundant vacancies in the etched Ru/Fe oxide nanoassemblies (E-Ru/Fe ONAs). Owing to the etching of Fe, the local electron density of the lattice O associated with Ru atoms is significantly increased, resulting in the suppression of $H_2O$ adsorption on lattice O. On the other hand, the O vacancies in the E-Ru/Fe ONAs can promote the $H_2O$ adsorption on metal atoms (*i.e.*, Ru and Fe). Consequently, the optimized E-Ru/Fe ONAs exhibit a superior OER activity with a low overpotential of 238 mV at 10 mA $cm^{-2}$ in 0.5 M $H_2SO_4$, and an enhanced stability with a negligible potential change within 9 h chronopotentiometry test. Theoretical calculations demonstrate that the defective surface of E-Ru/Fe ONA can not only enhance the stability via surface structural modulation, but also optimize the binding strength of the intermediates for promoting OER activity. This work provides an efficient strategy for fabricating active and stable $RuO_2$-based catalysts for OER, which may deepen the research in surface engineering of catalysts.

## 1. Introduction

Electrocatalytic water splitting is a potential strategy for converting renewable electricity to value-added $H_2$ fuel.[1−3] As a key half reaction, oxygen evolution reaction (OER) is the bottleneck of the overall water splitting because of the large overpotential required.[4,5] The slow four-electron transfer process involved in the OER requires efficient catalysts with superior activity and enhanced stability.[6−8] Over the past decades, tremendous efforts have been devoted to designing

potential catalysts for OER,[9,10] but the OER performance is still far from satisfactory for practical applications. The quest for efficient OER catalysts is driven by the current disadvantages of low activity and/or poor stability.

$RuO_2$- and $IrO_2$-based catalysts have been widely used as robust catalysts for OER due to their promising catalytic performance.[11,12] Among these catalysts, $RuO_2$ has been regarded as promising OER catalyst because of its lower price but higher activity in comparison to $IrO_2$.[13,14] Nevertheless, $RuO_2$ is suffering from the disadvantages of poor stability in acidic conditions due to the readily dissolution.[15,16] For instance, Hodnik and co-workers reported that the lattice O in $RuO_2$ is involved in OER, leading to the generation of low-coordinated Ru atoms that are highly prone to dissolution during electrocatalysis in acidic conditions.[17] To improve the stability of $RuO_2$-based catalysts, great efforts have been devoted to suppressing the involvement of lattice O in $RuO_2$. It has been reported that the increase in the electron density of lattice O can weaken the $H_2O$ adsorption, resulting in the preferential adsorption of $H_2O$ on metal atoms other than the lattice O. However, this strategy may strongly sacrifice activity for stability, since the lattice O can significantly promote the OER activity.[18−20] To achieve high-efficiency OER over $RuO_2$-based catalysts, a well balance of activity and stability is significant and yet challenging.

Herein, we demonstrate a facile strategy for fabricating a highly active and stable Ru/Fe oxide-based catalyst for acidic OER via a partial etching strategy, in which pristine Ru/Fe nanoassemblies (P-Ru/Fe NAs) were etched by $HNO_3$ to remove partial Fe species and then annealed in air, resulting in the formation of etched Ru/Fe oxide nanoassemblies (E-Ru/Fe ONAs) with abundant Fe and O vacancies. Owing to the etching of Fe, the local electron density of the lattice O associated with Ru atoms is significantly enhanced, leading to the suppression of $H_2O$ adsorption on lattice O. On the other hand, the O vacancies in the E-Ru/Fe ONAs can further

promote the $H_2O$ adsorption on metal atoms (*i.e.*, Ru and Fe). Therefore, the optimized E-Ru/Fe ONAs exhibits superior OER activity and stability in 0.5 M $H_2SO_4$. Theoretical calculations unravel that the defective surface of E-Ru/Fe ONAs can not only modulate the electronic environments of the nanoassembly surfaces for enhancing the stability of catalyst, but also optimize the binding strength of the intermediates for promoting OER activity. This work may not only provide an efficient strategy for stabilizing $RuO_2$-based catalysts for OER, but also shed new light on defect engineering of catalysts.

## 2. Results and discussion

### *2.1 Structural analysis*

The preparation procedure of E-Ru/Fe ONAs supported on carbon black (E-Ru/Fe ONAs/C) was shown in Fig. 1a. Detailed information was given in the experimental section in supporting information. High-angle annular dark-field scanning transmission electron microscopy (HAADF-STEM) and high-magnification TEM images show that the obtained P-Ru/Fe NAs consist of abundant ultrathin subunits (Figs. 1b, c, and S1a). The atomic ratio of Ru/Fe in the P-Ru/Fe NAs is 3.2/1, as confirmed by energy dispersive X-ray (EDX) spectroscopy measurement (Fig. S1b). No obvious changes in the morphology and composition after annealing at 250 °C for 1 h in air to generate pristine Ru/Fe oxide nanoassemblies (P-Ru/Fe ONAs) (Fig. S2). In the etched sample (*i.e.*, E-Ru/Fe ONAs), TEM image shows that the morphology of Ru/Fe ONAs is maintained, while the ratio of Ru/Fe in E-Ru/Fe ONAs increases from 3.2/1 to 6.4/1 (Figs. 1d and S3a). HAADF-STEM-EDS elemental mappings and HAADF-STEM line-scanning profiles indicate that Ru and Fe atoms are uniformly distributed in the E-Ru/Fe ONAs (Figs. 1e and S3b). In X-Ray diffraction (XRD) patterns, the characteristic peaks of $RuO_2$ in both P-Ru/Fe ONAs and E-Ru/Fe

ONAs slightly shift to larger angle in comparison to $RuO_2$ reference, suggesting the lattice contraction of $RuO_2$ in the presence of Fe in P-Ru/Fe ONAs and E-Ru/Fe ONAs (Fig. 1f). Moreover, defects including grain boundaries and dislocations are obviously observed in HRTEM images, as displayed in Figs. 1h and i. The lattice distance of 0.24 nm and 0.21 nm are close to $RuO_2$ (101) facet and (200) facet, respectively (Figs. 1g and h).

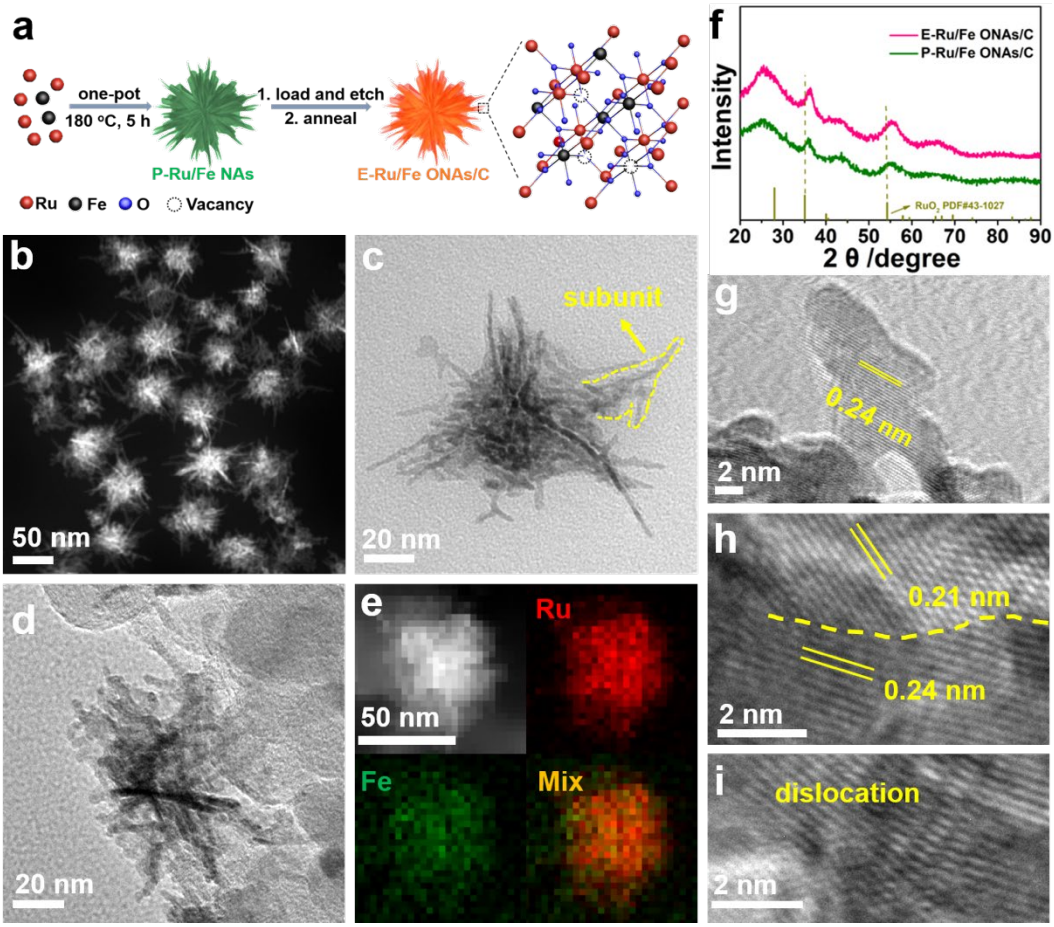


**Fig. 1.** (**a**) Schematic illustration of E-Ru/Fe ONAs preparation. (**b**) HAADF-STEM image, (**c**) high-magnification TEM image of P-Ru/Fe NAs. (**d**) High-magnification TEM image, (**e**) HAADF-STEM-EDS elemental mappings, (**f**) XRD pattern and (**g, h, i**) HRTEM images of E-Ru/Fe ONAs.

X-ray photoelectron spectrum (XPS) measurement was carried out to reveal the surface properties of P-Ru/Fe ONAs/C and E-Ru/Fe ONAs/C, as shown in Fig. 2a. For P-Ru/Fe ONAs/C, the peaks at binding energy (BE) of 461.6, 463.2 and 466.5 eV can be assigned as $Ru^0$, $Ru^{4+}$ and $Ru^{n+}$ (n>4), respectively. Notably, the corresponding peaks of $Ru^0$, $Ru^{4+}$ and $Ru^{n+}$ (n>4) in the XPS of E-Ru/Fe ONAs/C shift to higher BEs in comparison to P-Ru/Fe ONAs/C (*e.g.*, 461.8, 463.4 and 466.7 eV, respectively), suggesting the lower electron density of Ru in E-Ru/Fe ONAs/C. Four peaks are observed at 529.9, 531.5, 532.7, and 533.8 eV in the O 1s spectra, which can be ascribed to the lattice O, oxygen lattice sites located in the vicinity of O vacancies, surface-adsorbed $O_2$, and adventitious species, respectively (Fig. 2b).[21,22] Interestingly, the electron density of lattice O in E-Ru/Fe ONAs/C is higher than those of P-Ru/Fe ONAs/C. Moreover, detailed XPS analysis shows that the content of O vacancies in E-Ru/Fe ONAs/C is much higher than P-Ru/Fe ONAs/C (61% vs. 51%), indicating that the etching of Fe is in favour of generating O vacancies (Fig. S4). Room temperature photoluminescence (PL) spectra were further employed to confirm the existence of O vacancies, in which the PL emission peak at 403 nm (E-Ru/Fe ONAs/C) and 404 nm (P-Ru/Fe ONAs/C) can be indexed as the recombination of the photogenerated hole with the two-electron-trapped O-vacancy (Fig. 2c).[22,23] We further carried out the electron spin resonance (ESR) measurement for E-Ru/Fe ONAs/C and P-Ru/Fe ONAs/C. As shown in Fig. 2d, the corresponding signal in E-Ru/Fe ONAs/C ($g$ = 2.1317) was narrower and weaker than that of P-Ru/Fe ONAs/C ($g$ = 2.0911), which is due to the fact that, in addition to O vacancies, $Fe^{3+}$ could also generate ESR signal with broad spectrum owing to the paramagnetic nature.[24,25]

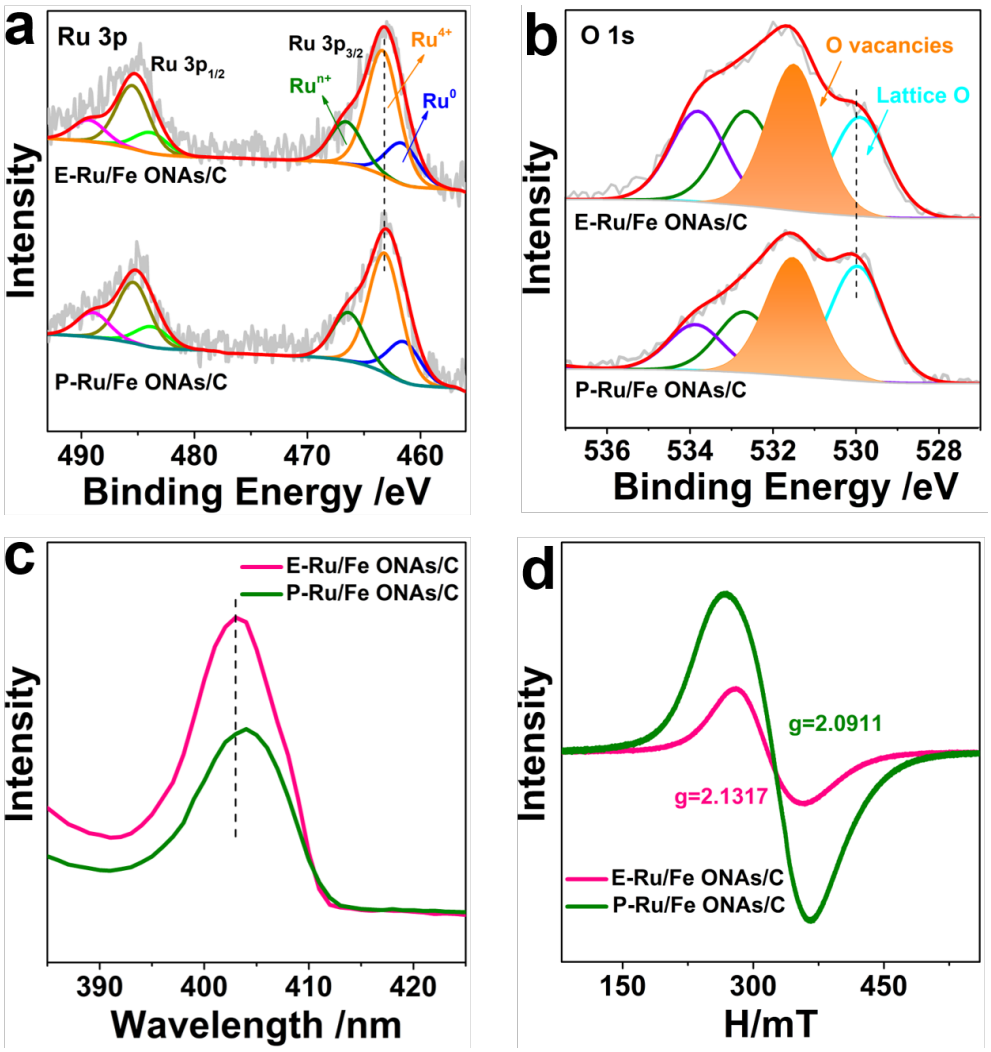


**Fig. 2.** (**a**) Ru 3p XPS, (**b**) O 1s XPS, (**c**) room-temperature photoluminescence and (**d**) electron spin resonance spectra of E-Ru/Fe ONAs/C and P-Ru/Fe ONAs/C.

*2.2 OER performance*

The acidic OER performance of E-Ru/Fe ONAs/C was evaluated in 0.5 M and 0.05 M $H_2SO_4$, while P-Ru/Fe ONAs/C, commercial $IrO_2$ and $RuO_2$ were used as references. All the electrocatalysts experienced 10 cycles of cyclic voltammetry (CV) before testing the linear sweep voltammetry (LSV) curve (Figs. 3a and b). As shown in Fig. 3c, the overpotential of E-Ru/Fe ONAs/C at 10 mA $cm^{-2}$ in 0.5 M $H_2SO_4$ is 238 mV, which is much lower than that of P-Ru/Fe

ONAs/C (252 mV), commercial $IrO_2$ (315 mV) and $RuO_2$ (354 mV), suggesting that E-Ru/Fe ONAs/C has the highest OER activity. Further decrease the concentration of $H_2SO_4$ to 0.05 M, the overpotentials of E-Ru/Fe ONAs/C, P-Ru/Fe ONAs/C, commercial $IrO_2$ and $RuO_2$ are 247, 260, 347 and 439 mV, respectively, indicating that E-Ru/Fe ONAs/C can be used as a robust electrocatalyst for acidic OER (Fig. 3c). Moreover, the current densities of commercial $IrO_2$ and $RuO_2$ are extremely low (close to 1.6 mA $cm^{-2}$) at a potential of 1.50 V (*vs.* RHE) in 0.5 M $H_2SO_4$ (Fig. 3d). The current density dramatically increases to 21.5 mA $cm^{-2}$ when P-Ru/Fe ONAs/C was used as catalyst, which further jumps to 37.6 mA $cm^{-2}$ when E-Ru/Fe ONAs/C was used as catalyst in 0.5 M $H_2SO_4$. Similar tendency was observed when the concentration of $H_2SO_4$ was decreased to 0.05 M, further confirming the superior OER activity of E-Ru/Fe ONAs/C. Furthermore, the Tafel slopes were calculated to study the kinetics of various catalysts during OER. The Tafel slopes of E-Ru/Fe ONAs/C are 44.8 and 56.8 mV $dec^{-1}$ in 0.5 and 0.05 M $H_2SO_4$, respectively, which are smaller than those of P-Ru/Fe ONAs/C, commercial $IrO_2$ and $RuO_2$ under the same conditions (Fig. S5). In addition, the stability of E-Ru/Fe ONAs/C was tested in 0.5 M $H_2SO_4$. As shown in Fig. 3e, E-Ru/Fe ONAs/C exhibits enhanced stability with a slight potential increase within 9 h. By contrast, P-Ru/Fe ONAs/C, commercial $IrO_2$ and $RuO_2$ exhibit much poorer stability under such corrosive environment. The above results demonstrate that E-Ru/Fe ONAs/C can be used as a highly active and stable catalyst for acidic OER.

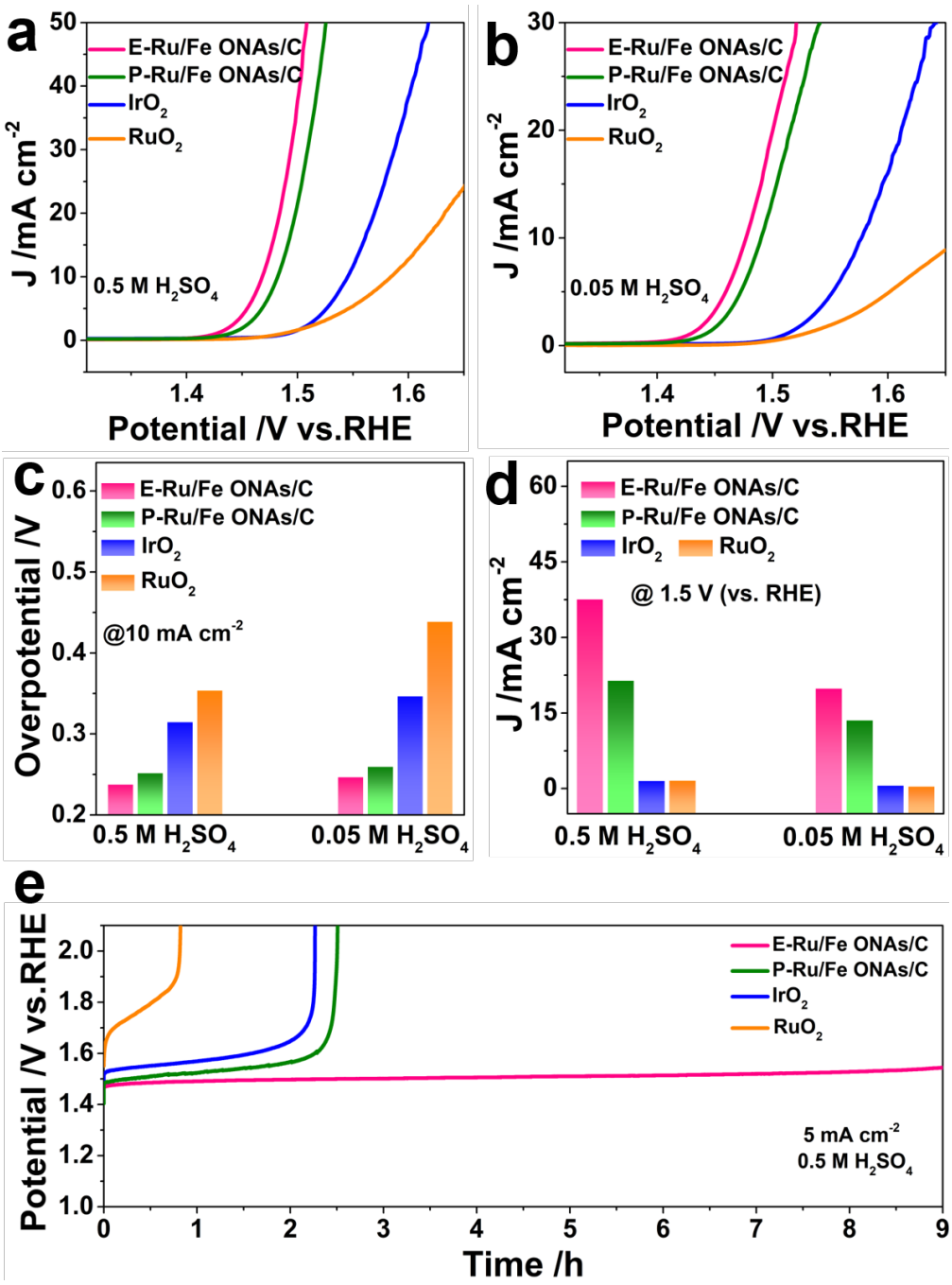


**Fig. 3.** The LSV curves in (**a**) 0.5 M and (**b**) 0.05 M $H_2SO_4$. (**c**) The overpotentials at 10 mA $cm^{-2}$ and (**d**) current densities at potential of 1.5 V (vs. RHE) of E-Ru/Fe ONAs/C, P-Ru/Fe ONAs/C, commercial $IrO_2$ and $RuO_2$ in 0.5 M and 0.05 M $H_2SO_4$. (**e**) Stability tests over different catalysts in 0.5 M $H_2SO_4$.

*2.3 Mechanism study*

To further unravel the origin of the superior activity of E-Ru/Fe ONAs/C, double layer capacitance ($C_{dl}$) method was employed to evaluate the electrochemical active surface area (ECSA). The calculated $C_{dl}$ of E-Ru/Fe ONAs/C (14.3 mF $cm^{-2}$), which is linearly proportional to ECSA, is obviously larger than that of P-Ru/Fe ONAs/C (10.9 mF $cm^{-2}$) (Figs. 4a and S6).[26] Moreover, the electrochemical impedance spectrum (EIS) of E-Ru/Fe ONAs/C with a smaller semicircle suggests a faster charge transfer rate at interface of electrode and electrolyte (Fig. 4b). This enhancement can be attributed to the generation of vacancies in the E-Ru/Fe ONAs/C after Fe etching, where the vacancies are in favour of increasing the conductivity of electrocatalyst.[27,28] To be more specific, E-Ru/Fe ONAs/C contains more defects than P-Ru/Fe ONAs/C, leading to the different electronic structures of catalysts. TEM image of the spent E-Ru/Fe ONAs indicates that the morphology is maintained, despite slight Fe dissolution occurs during OER test (Figs. S7a and b). Moreover, no obvious changes are observed in XRD pattern and XPS of the spent catalyst, suggesting that E-Ru/Fe ONAs/C is stable during electrochemical test (Figs. S7c and d). The fitting of XPS shows the proportions of lattice O in the fresh and spent E-Ru/Fe ONAs/C are 39% and 37%, respectively (Figs. 4c and d). By contrast, the proportions of lattice O in the fresh P-Ru/Fe ONAs/C and spent P-Ru/Fe ONAs/C are 49% and 26%, respectively, suggesting that the lattice O in P-Ru/Fe ONAs/C is largely involved in OER, as a result of poor stability in 0.5 M $H_2SO_4$. To further reveal the mechanism, the content of Ru and Fe in the fresh and spent catalysts were calculated. As shown in Fig. S8, the Fe content is 23.8% in the fresh P-Ru/Fe ONAs/C, which is obviously higher than that in the fresh E-Ru/Fe ONAs/C (13.6%), indicating that partial Fe is etched by $HNO_3$. After OER test, the Fe content in the spent P-Ru/Fe ONAs/C and E-Ru/Fe ONAs/C is 19.9% and 10.4%, respectively. Considering the similar Fe

dissolution during OER test (*e.g.*, 3.2% for E-Ru/Fe ONAs/C and 3.9% for P-Ru/Fe ONAs/C), we may conclude the significant difference in stability of E-Ru/Fe ONAs/C and P-Ru/Fe ONAs/C is caused by the involvement of lattice O in P-Ru/Fe ONAs/C. In particular, the lattice O of $RuO_2$ in P-Ru/Fe ONAs/C strongly involves in the OER, leading to a significant decrease of the lattice O ratio after OER test (Fig. 4d). In contrast, abundant vacancies in the E-Ru/Fe ONAs/C dramatically suppress the adsorption of $H_2O$ on the lattice O, leading to the enhanced stability of E-Ru/Fe ONAs/C.

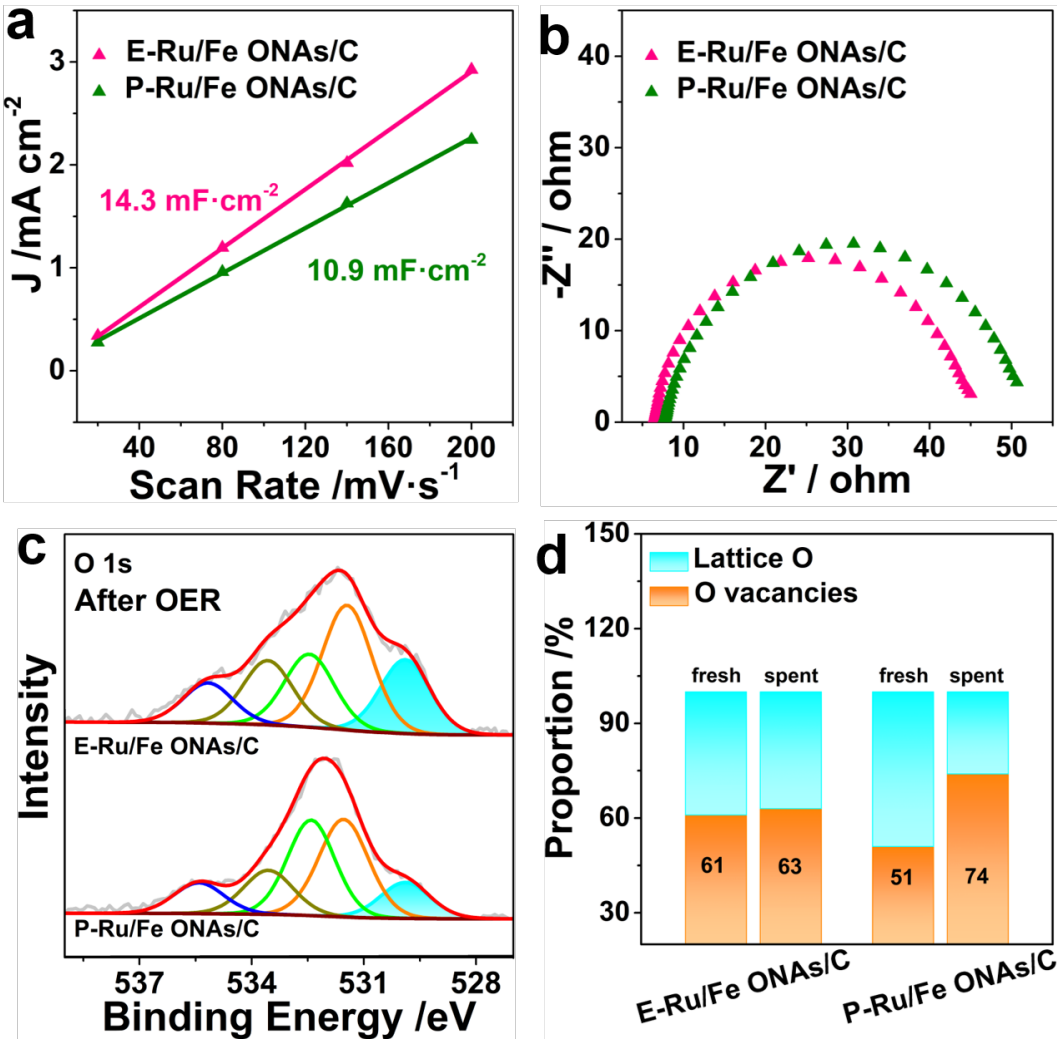

**Fig. 4.** (**a**) $C_{dl}$ and (**b**) EIS Nyquist plots of E-Ru/Fe ONAs/C and P-Ru/Fe ONAs/C. (**c**) O 1s XPS of the spent E-Ru/Fe ONAs/C and P-Ru/Fe ONAs/C, (**d**) the corresponding distributions of lattice O and O vacancies in the fresh and spent catalysts.

*2.4 Theoretical calculation*

Density functional theory (DFT) calculations were further conducted to unravel the superior performances of acidic OER over E-Ru/Fe ONAs. Considering the defective structure of E-Ru/Fe ONAs, an atomic structure with low-coordinated Ru and Fe sites was selected to mimic the surface structure of catalyst, as depicted in Fig. 5a. The active bonding and anti-bonding near Fermi level ($E_F$) were illustrated by the real spatial 3D contour plot of the electronic distribution, in which the electroactive region was located near the Ru-Fe regions (Fig. 5b). The projected partial density of states (PDOSs) was demonstrated to reveal the modification of electronic structures. For the Fe sites, the gradually enlarged $t_{2g}$-$e_g$ splitting is noticed from the bulk Fe to the surface oxidized Fe. The abundant empty *d*-bands of surface Fe sites facilitate the *p*-*d* couplings of Ru with the intermediates during OER (Fig. 5c). On the contrary, the electronic structures of Ru sites show a converse compress trend, where the Ru-4*d* bands become more concentrated with upshifting towards the $E_F$. The compensated electronic structure of Ru and Fe not only modulates the electronic environments of catalyst surface but also optimizes the binding strength of the intermediates (Fig. 5d). Moreover, the O-sites display limited changes from bulk to the surface. Even for the low-coordinated O sites on the surface, the O-2*p* orbitals only slightly shift from $E_V$-5.4 eV to $E_V$-4.5 eV, preserving the electron-rich states (Fig. 5e). Benefiting from the relatively stable electronic structure of O sites, the E-Ru/Fe ONAs may exhibit an enhanced stability during OER test, which is in good agreement with experimental observations (Fig. 3e). Moreover, the shift of the *s, p* orbitals of $H_2O$ confirms the strong adsorption of the reactants induced by the

enhanced *p-d* couplings, and the positive shift of the dominant peak of key intermediates during OER process further suggests the superior OER performance over E-Ru/Fe ONAs (Fig. 5f). Furthermore, the energy barriers of different reaction pathways were calculated. As shown in Fig. 5g, the step from [$O^*$ + 2H + $H_2O$] to [$^*OOH$ + 3H] is the rate-determining step (RDS) under the equilibrium potential (U = 0 V), which gives the largest energy barrier. It is noted that the energy barrier of RDS on E-Ru/Fe ONAs is 1.44 eV, which is obviously lower than that on $RuO_2$ (1.85 eV). Moreover, with the applied potential of 1.23 V, the overpotentials of OER on $RuO_2$ and E-Ru/Fe ONAs are 0.62 V and 0.21 V, respectively, further confirming the higher OER activity of E-Ru/Fe ONAs in comparison to $RuO_2$ (Fig. 5h). In addition, DFT calculations indicate that the interface of Ru-Fe oxides with abundant vacancies favors the adsorption of $H_2O$, leading to the modulated binding strength of intermediates on the catalyst and thus variable OER activity (Fig. 5i).

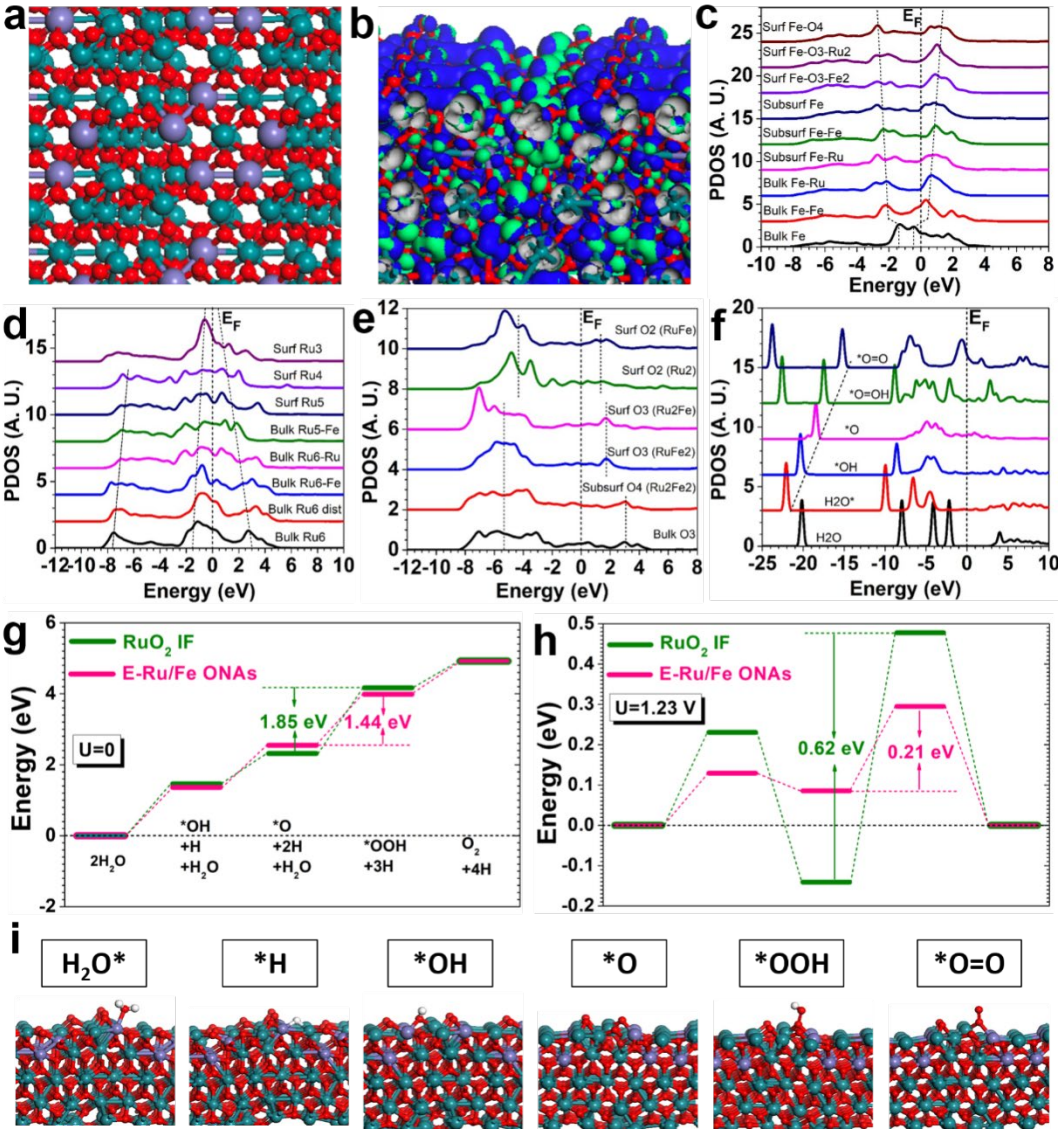


**Fig. 5.** (**a**) The top view of the E-Ru/Fe ONAs lattice structure. Green balls = Ru, Purple balls = Fe and Red balls = O. (**b**) The real spatial contour plots for bonding and anti-bonding orbitals near $E_F$. (**c**) The site-dependent PDOSs of Fe from the surfaces to the bulk states. (**d**) The site-dependent PDOSs of Ru from the surfaces to the bulk states. (**e**) The site-dependent PDOSs of O sites from the surfaces to the bulk states. (**f**) PDOSs of O-intermediates during the acidic OER process. (**g**) The pathways of four-electron based acidic OER at U=0 V. (**h**) The OER pathways and overpotential at U=1.23 V. (**i**) The structural configurations of intermediates adsorption. Green balls = Ru, Purple balls = Fe, Red balls = O and White balls = H.

## 3. Conclusion

In conclusion, we demonstrate a facile strategy for fabricating a highly active and stable Ru/Fe oxide-based catalyst for acidic OER, in which Ru/Fe NAs were etched by $HNO_3$ to remove partial Fe species and then annealed in air resulting in the formation of Fe and O vacancies (*i.e.*, E-Ru/Fe ONAs). Detailed characterizations and experiments suggest the vacancies in the E-Ru/Fe ONAs can not only promote the OER activity, but also greatly enhance the stability of catalyst in acidic conditions via suppressing the involvement of lattice O in OER process. DFT calculations indicate that the interface of Ru-Fe oxides with abundant vacancies in E-Ru/Fe ONAs can not only modulate the electron density of lattice O to prevent $RuO_2$ from dissolution, but also optimize the binding strength of the intermediates to promote the OER activity. This work may not only provide an efficient strategy for stabilizing $RuO_2$-based catalysts for OER, but also shed new light on defect engineering of catalysts.

## Acknowledgment

This work was financially supported by the Ministry of Science and Technology (2016YFA0204100, 2017YFA0208200), the National Natural Science Foundation of China (21571135, 51802206, 21771156), Young Thousand Talented Program, Jiangsu Province Natural Science Fund for Distinguished Young Scholars (BK20170003), Natural Science Foundation of Jiangsu Province (BK20180846), the Priority Academic Program Development of Jiangsu Higher Education Institutions (PAPD), and the start-up funding from Xiamen University.

## References

[1]. J. Xu, D. Aili, Q. Li, E. Christensen, J. O. Jensen, W. Zhang, M. K. Hansen, G. Liu, X. Wang, N. J. Bjerrum, Oxygen evolution catalysts on supports with a 3-D ordered array structure and

intrinsic proton conductivity for proton exchange membrane steam electrolysis, Energy Environ. Sci. 7 (2014) 820−830.

[2]. J. Kibsgaard, T. F. Jaramillo, Molybdenum phosphosulfide: an active, acid-stable, earth-abundant catalyst for the hydrogen evolution reaction, Angew. Chem. Int. Ed. 53 (2014) 14433−14437.

[3]. J. A. Turner, Sustainable hydrogen production, Science 305 (2004) 972−974.

[4]. Y. Jiao, Y. Zheng, M. Jaroniec, S. Qiao, Design of electrocatalysts for oxygen- and hydrogen-involving energy conversion reactions, Chem. Soc. Rev. 44 (2015) 2060−2086.

[5]. J. H. Montoya, L. C. Seitz, P. Chakthranont, A. Vojvodic, T. F. Jaramillo, J. K. Nørskov, Materials for solar fuels and chemicals, Nat. Mater. 16 (2016) 70−81.

[6]. C. Feng, M. B. Faheem, J. Fu, Y. Xiao, C. Li, Y. Li, Fe-Based electrocatalysts for oxygen evolution reaction: progress and perspectives, ACS Catal. 10 (2020) 4019−4047.

[7]. N. T. Suen, S. F. Hung, Q. Quan, N. Zhang, Y. J. Xu, H. M. Chen, Electrocatalysis for the oxygen evolution reaction: recent development and future perspectives, Chem. Soc. Rev. 46 (2017) 337−365.

[8]. E. Fabbri, A. Habereder, K. Waltar, R. Kötza, T. J. Schmidt, Developments and Perspectives of oxide-based catalysts for the oxygen evolution reaction. Catal. Sci. Technol. 4 (2014) 3800−3821.

[9]. N. Danilovic, R. Subbaraman, K. C. Chang, S. H. Chang, Y. Kang, J. Snyder, A. P. Paulikas, D. Strmcnik, Y. T. Kim, D. Myers, V. R. Stamenkovic, N. M. Markovic, Using surface segregation to design stable Ru-Ir oxides for the oxygen evolution reaction in acidic environments, Angew. Chem. Int. Ed. 53 (2014) 14016−14021.

[10]. L. Yang, G. Yu, X. Ai, W. Yan, H. Duan, W. Chen, X. Li, T.Wang, C. Zhang, X. Huang, J. Chen, X. Zou, Efficient oxygen evolution electrocatalysis in acid by a perovskite with face-sharing $IrO_6$ octahedral dimers, Nat. Commun. 9 (2018) 5236.

[11]. J. Shan, C. Guo, Y. Zhu, S. Chen, L. Song, M. Jaroniec, Y. Zheng, S. Qiao, Charge-redistribution-enhanced nanocrystalline Ru@$IrO_x$ electrocatalysts for oxygen evolution in acidic media, Chem 5 (2019) 445−459.

[12]. R. Ge, L. Li, J. Su, Y. Lin, Z. Tian, L. Chen, Ultrafine defective $RuO_2$ electrocatalyst integrated on carbon cloth for robust water oxidation in acidic media, Adv. Energy Mater. (9) 2019 1901313.

[13]. K. A. Stoerzinger, R. R. Rao, X. R. Wang, T. H. Wesley, M. R. Christopher, S. H. Yang, The role of Ru redox in pH-dependent oxygen evolution on rutile ruthenium dioxide surfaces, Chem. 2 (2017) 668−675.

[14]. K. Sardar, E. Petrucco, C. I. Hiley, J. D. B. Sharman, P. P. Wells, A. E. Russell, R. J. Kashtiban, J. Sloan, R. I. Walton, Water-splitting electrocatalysis in acid conditions using ruthenate-iridate pyrochlores, Angew. Chem. Int. Ed. 53 (2014) 10960−10964.

[15]. E. A. Paoli, F. Masini, R. Frydendal, D. Deiana, C. Schlaup, M. Malizia, T. W. Hansen, S. Horch, I. E. L. Stephens, I. Chorkendorff, Oxygen evolution on well-characterized mass-selected Ru and $RuO_2$ nanoparticles, Chem. Sci. 6 (2015) 190−196.

[16]. X. Kong, K. Xu, C. Zhang, J. Dai, S. N. Oliaee, L. Li, X. Zeng, C. Wu, Z. Peng, Free-standing two-dimensional Ru nanosheets with high activity toward water splitting, ACS Catal. 6 (2016) 1487−1492.

[17]. N. Hodnik, P. Jovanovič, A. Pavlišič, B. Jozinović, M. Zorko, M. Bele, V. S. Šelih, M. Šala, S. Hočevar, M. Gaberšček, New insights into corrosion of ruthenium and ruthenium oxide nanoparticles in acidic media, J. Phys. Chem. C. 119 (2015) 10140−10147.

[18]. A. Grimaud, O. Diaz-Morales, B. Han, T. H. Wesley, Y. L. Lee, L. Giordano, K. A. Stoerzinger, T. M. K. Marc, S. H. Yang, Activating lattice oxygen redox reactions in metal oxides to catalyse oxygen evolution, Nat. Chem. 9 (2017) 457−465.

[19]. Z. F. Huang, J. Song, Y. Du, S. Xi, S. Dou, J. M. V. Nsanzimana, C. Wang, Z. J. Xu, X. Wang, Chemical and structural origin of lattice oxygen oxidation in Co–Zn oxyhydroxide oxygen evolution electrocatalysts, Nat. Energy. 4 (2019) 329−338.

[20]. X. Wang, Z. Pan, X. Chu, K. Huang, Y. Cong, R. Cao, R. Sarangi, L. Li, G. Li, S. Feng, Atomic-scale insights into surface lattice oxygen activation at the spinel/perovskite interface of $Co_3O_4$/$La_{0.3}$ $Sr_{0.7}$ $CoO_3$, Angew. Chem. Int. Ed. 58 (2019) 11720−11725.

[21]. J. Bao, X. Zhang, B. Fan, J. Zhang, M. Zhou, W. Yang, X. Hu, H. Wang, B. Pan, Y. Xie, Ultrathin spinel-structured nanosheets rich in oxygen deficiencies for enhanced electrocatalytic water oxidation, Angew. Chem. Int. Ed. 54 (2015) 7399−7404.

[22]. L. Zhuang, L. Ge, Y. Yang, M. Li, Y. Jia, X. Yao, Z. Zhu, Ultrathin iron-cobalt oxide nanosheets with abundant oxygen vacancies for the oxygen evolution reaction, Adv. Mater. 29 (2017) 1606793.

[23]. F. Lei, Y. Sun, K. Liu, S. Gao, L. Liang, B. Pan, Y. Xie, Oxygen vacancies confined in ultrathin indium oxide porous sheets for promoted visible-light water splitting, J. Am. Chem. Soc. 136 (2014) 6826−6829.

[24]. H. Wang, D. Yong, S. Chen, S. Jiang, X. Zhang, W. Shao, Q. Zhang, W. Yan, B. Pan, Y. Xie, Oxygen-vacancy-mediated exciton dissociation in BiOBr for boosting charge-carrier-involved molecular oxygen activation, J. Am. Chem. Soc. 140 (2018) 1760−1766.

[25]. K. Zhu, T. Wu, M. Li, R. Lu, X. Zhu, W. Yang, Perovskites decorated with oxygen vacancies and Fe–Ni alloy nanoparticles as high-efficiency electrocatalysts for the oxygen evolution reaction, J. Mater. Chem. A 5 (2017) 19836−19845.

[26]. C. Wei, S. Sun, D. Mandler, X. Wang, S. Qiao, Z. J. Xu, Approaches for measuring the surface areas of metal oxide electrocatalysts for determining their intrinsic electrocatalytic activity, Chem. Soc. Rev. 48 (2019) 2518−2534.

[27]. X. Fan, Y. Liu, S. Chen, J. Shi, J. Wang, A. Fan, W. Zan, S. Li, W. A. Goddard III, X. Zhang, Defect-enriched Iron fluoride-oxide nanoporous thin films bifunctional catalyst for water splitting, Nat. Commun. (9) 2018 1809.

[28]. Y. Zhao, C. Chang, F. Teng, Y. Zhao, G. Chen, R. Shi, G. I. N. Waterhouse, W. Huang, T. Zhang, Defect-engineered ultrathin δ-$MnO_2$ nanosheet arrays as bifunctional electrodes for efficient overall water splitting, Adv. Energy Mater. 7 (2017) 1700005.